Liquid cell transmission electron microscopy sheds light on the mechanism of palladium electrodeposition

Journal:	*Langmuir*
Manuscript ID	la-2018-02846s.R2
Manuscript Type:	Article
Date Submitted by the Author:	n/a
Complete List of Authors:	Yang, Jie; McMaster University, Materials Science and Engineering Andrei, Carmen; McMaster University, CCEM Chan, Yuting; McMaster University, Engineering Physics Mehdi, B. Layla; University of Liverpool, Mechanical, Materials and Aerospace Eng Browning, Nigel; University of Liverpool, School of Engineering Botton, Gianluigi A.; McMaster University, Materials Science and Engineering Soleymani, Leyla; McMaster University, Engineering Physics

Liquid cell transmission electron microscopy sheds light on the mechanism of palladium electrodeposition

Jie Yang,[1] Carmen M. Andrei,[2] Yuting Chan,[3] B. Layla Mehdi,[4] Nigel D. Browning,[4,5] Gianluigi A. Botton[2,6] and, Leyla Soleymani*[1,3]*

[1.] School of Biomedical Engineering, McMaster University, Hamilton, Canada

[2.] Canadian Centre for Electron Microscopy, McMaster University, Hamilton, Canada

[3.] Department of Engineering Physics, McMaster University, Hamilton, Canada

[4.] Department of Mechanical, Materials and Aerospace Engineering, School of Engineering, University of Liverpool, Liverpool, United Kingdom.

[5.] Department of Physics, School of Physical Sciences, University of Liverpool, Liverpool, United Kingdom

[6.] Department of Materials Science and Engineering, McMaster University, Hamilton, Canada

* Address correspondence to: soleyml@mcmaster.ca, gbotton@mcmaster.ca

Abstract

Electrodeposition is widely used for fabricating tunable nanostructured materials in applications ranging from biosensing to energy conversion. A model based on 3D island growth is widely accepted in explaining the initial stages of nucleation and growth in electrodeposition. However, there are regions in the electrodeposition parameter space where this model becomes inapplicable. We use liquid cell transmission electron microscopy along with *post-situ* scanning electron microscopy to investigate electrodeposition in this parameter space, focusing on the effect of supporting electrolyte, and to shed light on the nucleation and growth of palladium. Using a collection of electron microscopy images and current time transients recorded during electrodeposition, we discover that electrochemical aggregative growth, rather than 3D island growth, best describes the electrodeposition process. We then use this model to explain the change in morphology of palladium electrodeposits from spherical to open clusters with non-spherical morphology when HCl is added to the electrolyte solution. The enhanced understanding of the early stages of palladium nucleation and growth and the role of electrolyte in this process provides a systematic route towards the electrochemical fabrication of nanostructured materials.

Introduction

Electrodeposition is a versatile method for fabricating coatings on conductive substrates. While traditionally this method has been used for creating aesthetic and/or anti-corrosion coatings in various manufacturing sectors; recently, there has been a rising interest in using electrodeposition for creating structures that are tunable over multiple length scales. The ability to create tunable nano and microscale structures and assemble them into three dimensional hierarchical architectures has proven to be critical in tuning the mechanical[1,2], electronic/electrochemical[3–5], optical[6–9], and surface properties[7] of materials. Consequently, simulations and experimental studies are being intensely performed in order to design structures that have ideal morphologies and length scales for use in applications ranging from tissue engineering to energy conversion. Manufacturing such structures containing micro and/or nanoscale components is often achieved using top-down or bottom-up processes, or their combination. Among these, electrodeposition is ideally suited for the large volume and low-cost fabrication of structures with simple (nanowires[12], nanosheets[13], hemispheres[14]) and complex (dendritic[15,16], fractal[17], acicular[18], globular assemblies[19]) architectures.

Due to its nobility, catalytic activity, and hydrogen reactivity, palladium is heavily investigated for use in emerging devices such as biosensors[3,20], biofuel cells[21], and hydrogen fuel cells[22,23]. Overpotential electrodeposition – deposition at potentials more negative than the equilibrium potential – of palladium is an effective strategy for developing 3D structures with tunable morphologies suitable for the abovementioned applications[24]. Structural tunability is achieved by varying the applied potential/current waveform and the composition of the electrodeposition bath. Hydrochloric acid (HCl) is used as an electrolyte for tuning the structure of various materials (platinum[25], palladium[24], copper[26,27], zinc oxide[28], nickel[29], etc.) in electrodeposition. The role of

HCl in structural tunability of metallic electrodeposits is attributed to the preferential adsorption of chloride on specific crystalline planes during deposition[30,31], the influence of bath pH on the equilibrium concentration of metallic ions in the solution[32], and the impact of HCl concentration on the overall deposition rate[33]. In spite of existing studies on HCl-mediated *structural tunability*, there is a need for additional studies on *structural evolution* of these electrodeposits to better understand how HCl varies the structure of electrodeposits. In order to focus on structural evolution, we used liquid cell transmission electron microscopy (TEM) to study the electrodeposition of palladium *in-operando* and in its native environment.

Liquid cell TEM has been used for studying the electrodeposition of copper[34–39], gold[40,41], and lead[42]. Many of these studies are focused on correlating the *in situ* images and the measured current time transients to the traditional electrodeposition models based on Volmer-Weber 3D island growth[43]. However, recent liquid cell[44] and identical location TEM[45] studies have shown that the assumptions of negligible lateral diffusion and interaction between adjacent nuclei are not valid during the initial stages of electrodeposition. Recently, a generalized electrochemical aggregative growth mechanism has been proposed for the overpotential electrodeposition of platinum, palladium, and silver on low surface energy substrates, which considers self-limited nanocluster growth, nanocluster surface diffusion, and coalescence as the processes involved in structural development of electrodeposits[46–49]. Here we develop an integrated approach combining liquid cell TEM, *post-situ* scanning electron microscopy (SEM), and electrochemical analysis to study the overpotential deposition of palladium on low energy surfaces, where the traditional nucleation and growth models are not applicable. This approach allows us to explain the mechanistic role of HCl in structural tunability in the context of the aggregative electrodeposition growth model.

Results and discussion

Palladium electrodeposition was performed using chronoamperometry, where a fixed DC potential was applied to the working electrode inside a liquid cell TEM setup. As shown in Figure 1, the system contained a miniaturized electrochemistry cell at the tip of a TEM holder, and was integrated with microfluidic and electrical circuitry. Using the microfluidic system, the electrolyte was flowed between two silicon nitride membranes, which permitted observation of the electrochemical reactions on the working electrode in *real-time*.

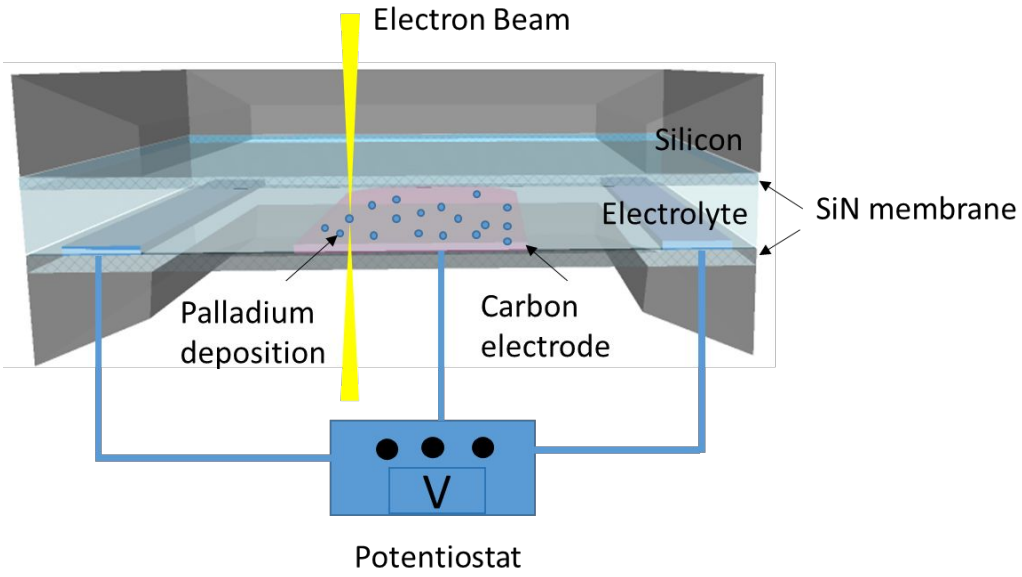

Figure 1. Schematic of the liquid cell TEM setup used for electrodeposition of palladium. The silicon chips have a silicon nitride membrane, and the bottom chip contains three electrodes (working, reference and counter) for performing electrochemistry. Palladium nanostructures are deposited on the carbon working electrode by applying a fixed potential.

To understand the effect of HCl on the structural evolution of palladium crystallites during electrodeposition, two different experiments were conducted. The first experiment was focused on the *in situ* electrodeposition of palladium on a carbon microelectrode from a solution of hydrogen chloropalladate (H_2PdCl_4), and the second one was performed by adding HCl to the H_2PdCl_4

precursor solution. We performed cyclic voltammetry in the two solutions and observed characteristic curves with peaks for palladium reduction, oxidation, and hydrogen adsorption/absorption and desorption (Supplementary Figure S1). Based on the measured open circuit potential and the CV profile, the overpotential used for in situ electrodeposition (-0.6 V versus Pt) was 0.605 V for 5 mM H_2PdCl_4 and 0.603 V for H_2PdCl_4 in 0.15 M HCl, which are both within the hydrogen adsorption/absorption region.

The time-resolved bright-field scanning transmission electron microscopy (BF-STEM) micrographs along with the current time transients (CTTs) obtained during these experiments are demonstrated in Figure 2 (the corresponding videos acquired during the *in situ* experiment are included as Supplementary Videos 1 and 2). In the case without HCl (Figure 2(a)), nucleation and growth were observed, initially (0-10 s), along the electrode edge. At deposition times of 30 s or larger, clusters started to appear on the inner electrode area. After 30 s of electrodeposition, palladium structures started to appear beyond the electrode edge. In the case with HCl, initially (0-10 s of deposition), the large majority of crystallites appeared along the edge of the electrode, and these edge-bound clusters finally grew into microscale clusters at 150 s. At longer times ($t \geq 10$ s), palladium deposits appeared in the inner area of the electrode; however, the amount of palladium (evaluated based on cluster size and surface density) electrodeposited in this area was significantly smaller than the amount present at the electrode edge at every time point. This behavior was also seen in the experiment without HCl; however, the enhanced deposition at the electrode edge is more pronounced in the case with HCl. Previous reports have indicated that the adsorption of chloride ions on the electrode surface retards the palladium electrodeposition process[33,50]. However, this effect is dependent on the electrodeposition overpotential: at high overpotentials, the chloride concentration at the electrode surface tends to decrease, diminishing the chloride-

related retardation process[33]. According to the electric field simulations performed on the miniaturized electrochemistry setup, we observe electric field enhancement at the electrode edges (Supplementary Figure S2). In both cases, with and without HCl, this field enhancement increases the deposition rate at the electrode edges. However, in the case with HCl, this field enhancement is expected to play an additional role, it overcomes the potential barrier caused by the adsorption of chloride ions at the electrode edge. This results in considerable difference in the amount of deposits present at the electrode edge and the inner electrode area.

Comparing the regions of the chip that were illuminated (Figure 2, 150 s) and were not illuminated (Figure 2, 150 s-no beam) by the electron beam during electrodeposition, we obtain interesting insights on the interplay between electrodeposition and electron beam-induced nucleation and growth. Under the influence of electron beam, the structures present at the electrode edge had a dendritic structure that is observed in diffusion-limited growth[51]. This is consistent with other reports suggesting that the electron beam can affect the electrochemical processes under investigation and increase the overall electrodeposition rate by generating reducing species through radiolysis[35,52], requiring the electron beam dose to be controlled to avoid local depletion of palladium ions[53,54]. Another observation that is solely relevant to the case without HCl is that under the direct influence of electron beam, deposits were present on the silicon nitride window beyond the boundary of the carbon electrode. This suggests that adding HCl to the electrodeposition bath reduces the rate of beam-induced nucleation and growth.

We believe that the electron beam impacts the electrodeposition process differently in solutions with and without HCl due to the differences in solution pH and chloride ion concentration. The interaction of the electron beam with aqueous solutions results in the generation of highly reactive oxidizing ($OH^{\cdot}$ and H_2O_2) and reducing (hydrated electrons, H, and H_2) species[55]. Previous studies

have shown that the ratio of hydrated electrons to hydroxide radicals decreases as the solution pH is decreased due to the rapid combination of hydrated electrons with hydrogen ions[52]. This suggests a decrease in beam-induced nucleation (*i.e.* beam-induced reduction of metallic ions) in solutions with a lower pH. Furthermore, in solutions with a high concentration of chloride ions, the primary radical $OH\cdot$ reacts with chloride ions resulting in the generation of Cl_2^- (equations (1) and (2)), which is an oxidizing agent[56].

$$OH\cdot + Cl^- + H^+ \rightarrow H_2O + Cl \qquad (1)$$

$$Cl + Cl^- \rightarrow Cl_2^- \qquad (2)$$

Consequently, we expect the solution containing HCl to result in an environment that is more oxidizing under the electron beam compared to the solution lacking HCl, making it more difficult for the beam induced reduction of metallic ions to occur.

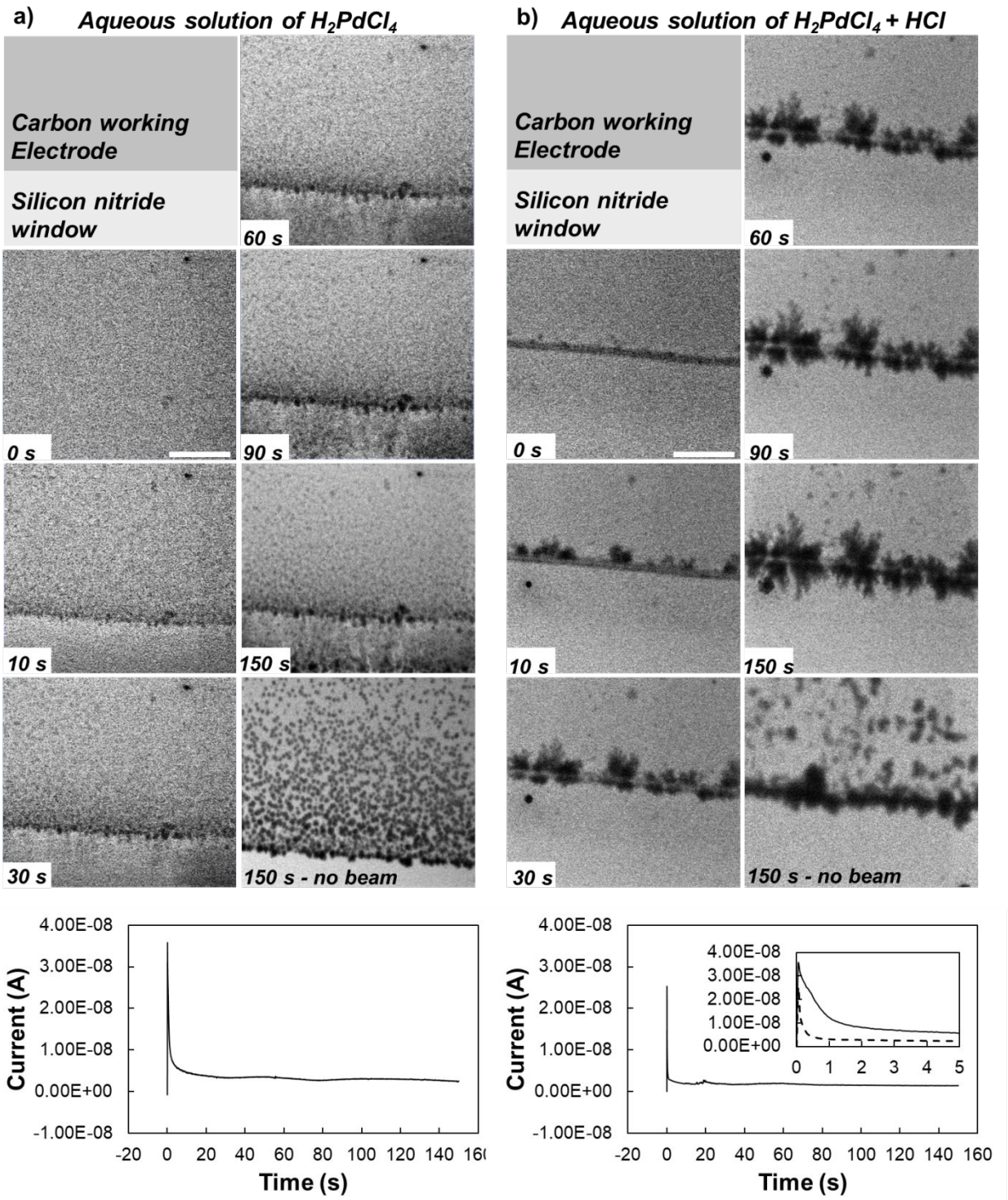

Figure 2. Electrodeposition of palladium inside liquid cell TEM with and without HCl. The top row schematic represents the orientation of microchips as seen in the images in this figure. BF-STEM

micrographs acquired at 0 s, 10 s, 30 s, 60 s, 90 s, and 150 s of deposition on a carbon electrode in a 5 mM M H_2PdCl_4 bath without (a) and with 0.015 M HCl (b) under an applied potential of -0.6 V versus on-chip platinum reference electrode, flow rate of 5 μL/min, and a beam dose of 21 electrons/frame. nm^2. The micrograph labeled as 150 s-no beam represents an image of an area of the chip not directly exposed to the electron beam following 150 s of electrodeposition. The image was acquired after turning off the electrical bias and replacing the electrodeposition bath with water. The bottom row represents the current time transients obtained during the liquid cell TEM experiments. The inset in the current time transients represents the 'with' (dotted) and 'without' (solid) HCl curves overlaid and zoomed in to show the first five seconds of deposition. Scale bar represents 1 μm.

To understand the cause of morphological differences induced by adding HCl, we compared the CTTs obtained during the *in situ* experiments of Figure 2. Since the chronoamperograms were obtained in the presence of the electron beam, we evaluated the effect of the beam on the shape of the acquired CTTs (Supplementary Figure S3). The curves obtained with and without the electron beam demonstrated very similar shapes indicating that the electron beam does not significantly alter the mechanism of electrodeposition. In addition, because the CTTs were obtained under fluidic flow, we performed a control experiment to compare the CTTs obtained with and without flow (Supplementary Figure S4). By introducing flow to the system, the measured current slightly increased, likely due to the enhanced mass transport; however introducing flow did not alter the shape of the acquired CTTs.

In both electrolytes, we observed a current decrease following the application of the potential step. In potential step experiments, this type of current decrease is often attributed to the double layer capacitive charging; however capacitive currents have time constants that are typically in the order of microseconds[57] rather than milliseconds or seconds. We sought to explain these results using the models developed by Scharifker and Hills (SH model). The SH model assumes that

hemispherical nuclei grow by direct attachment of ions, the ions are delivered to the nuclei by semi-infinite diffusion, and concentration of the electrodepositing ions is zero at the surface. The most significant feature of the SH model is that it predicts a current increase following the capacitive charging. This current increase is caused by the increase in the electroactive surface area as the number of nuclei increases and/or the nuclei grow in size[43]. This behaviour was not observed in the CTTs demonstrated in Figure 2, which could be due to the experimental conditions used here. While the SH model assumes electrodeposition to occur under diffusion control, convection and migration could contribute to mass transport in our experimental setup due to the fluidic flow inside the liquid cell and the small concentration of supporting electrolytes used. In addition, under high overpotential, it is possible to obtain a high density of nuclei that cover the entire surface and result in a decaying current. [58] Given that the current decay was observed in the presence and absence of flow (Supplementary Figure S4), with and without supporting electrolyte (Supplementary Figure S5), and with HCl where low coverage was observed, we turned to an alternative model based on electrochemical aggregative growth, which is applicable to CTTs with monotonically decreasing currents[46]. In electrochemical aggregative growth, electrodeposits are formed by self-limited growth of nanoclusters, overpotential-dependent nanocluster surface diffusion, and nanocluster coalescence/recrystallization[46–49]. This differs from the conventional electrochemical nucleation and growth theories in that, while primary nuclei grow by direct adatom attachment, beyond a critical diameter, they grow by nanocluster aggregation and coalescence. To evaluate the suitability of this model for explaining the measured CTTs, we imaged the microchips used in the liquid cell TEM experiments using scanning electron microscopy (SEM) after the electrodeposition process. The *post situ* SEM images (Figure 3) confirm the observations obtained from liquid cell TEM (Figure 2). The amount of deposits

increased at the electrode edge compared to the inner electrode area, and adding HCl to the electrodeposition bath changed the structures from spherical to non-spherical deposits. Additionally, SEM micrographs demonstrate that the deposited areas, in the case with and without HCl, contained small circular clusters (Supplementary Figure S6) even at long deposition times (150 s). This dispersion in cluster size has been previously observed and suggested[43,46] in the aggregative growth model. The observed dispersion in nanocluster size, in addition to the monotonically decreasing current in the CTT curves support the electrochemical aggregative growth model. However, it should be noted that the electrochemical aggregative growth model has not been previously studied when convection and migration contribute to mass transport in addition to diffusion. It is possible that electrochemical Ostwald ripening[59] and progressive nucleation and growth[43] also play a role in the growth of the clusters observed here; however, liquid-cell TEM does not provide us with the required spatial or temporal resolution to differentiate between these mechanisms.

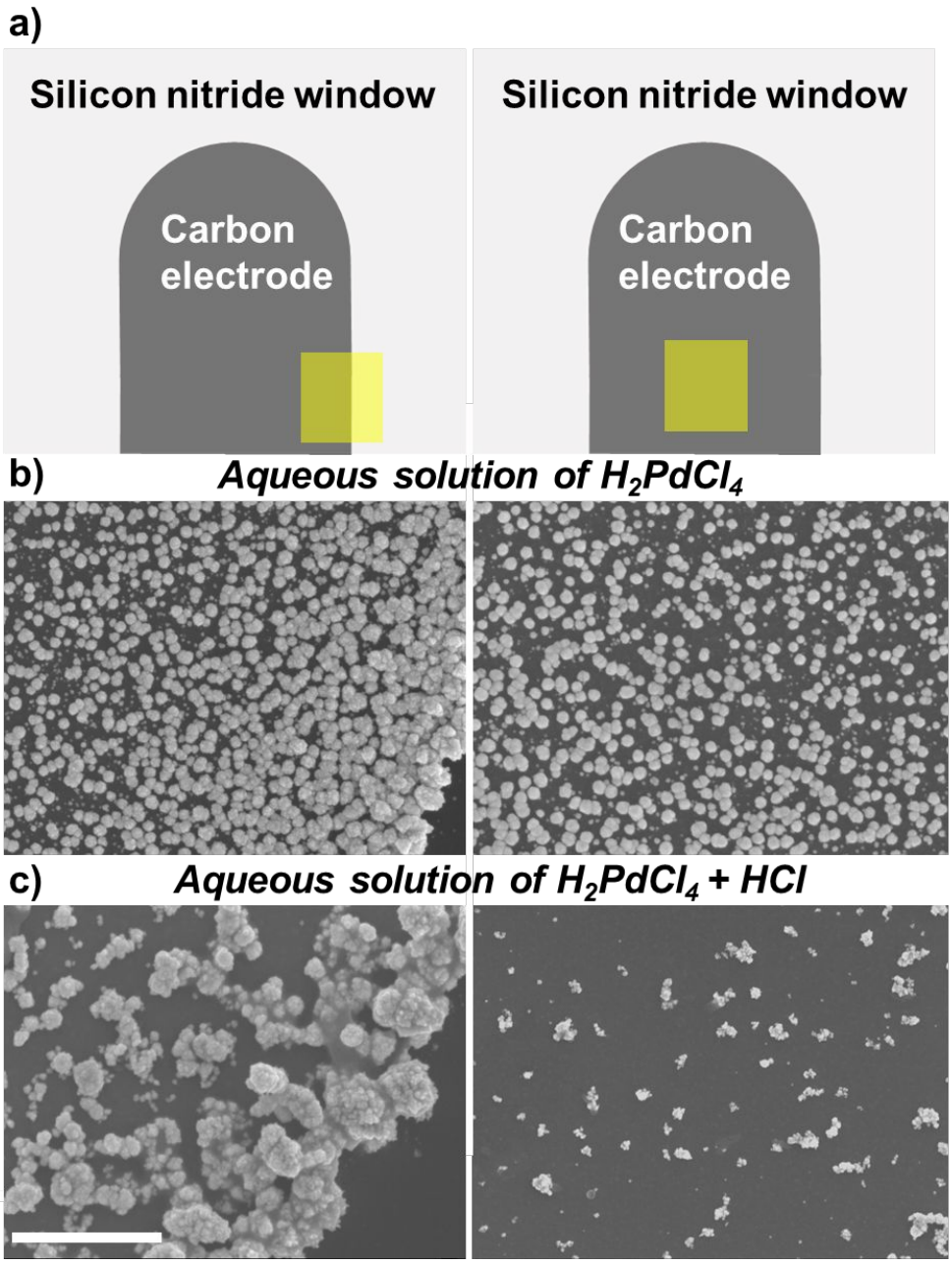

Figure 3. *Post situ* SEM imaging of the electrochemical chip used in liquid cell TEM experiment of Figure 2. The schematic drawing in (a) demonstrates the area imaged in (b) and (c). *Post situ* SEM micrographs of the chips used in Figure 2 without (b) and with (HCl). The images on the left demonstrate an area of the chip that contain the edge of the carbon electrode, while the images on the right show the middle part of the carbon electrode. Scale bar represents 1 μm.

Given the large electric fields experienced in miniaturized electrochemical cells (see simulations in Supplementary Figure S2), we looked into the potential effect of migration on the CTTs and images acquired during liquid-cell TEM experiments. For this purpose, we sought to eliminate migration effects by adding a large concentration of supporting electrolyte (500 mM KCl) to our H_2PdCl_4 baths (Supplementary Figure S5). Adding the supporting electrolyte significantly increased the magnitude of the current obtained during electrodeposition. In spite of this, the general shape of the CTTs and the morphology of the deposits did not change. Given our solution pH (≤ 2), $PdCl_4^{2-}$ is the dominant Pd (II) species[32]. As a result, under our biasing conditions (working electrode negatively biased with respect to the counter electrode), migration effects would decrease the flux of these species to the negatively biased working electrode. It is possible that under electrochemical aggregative growth, migration effects do not significantly affect the morphology of the deposits because processes such as surface diffusion, aggregation, and recrystallization occur at or near the electrode, whereas migration mostly affects mass transport in the bulk.

After selecting a suitable theory for explaining the nucleation and growth of palladium clusters, we used this model to explain the role of HCl on the morphological development of the clusters. Previous studies suggest that recrystallization and coalescence kinetics, to a large extent, dictate the morphology of the final electrodeposits[46]. Without HCl, we observed spherical clusters that were less porous and smoother than with HCl. Including HCl in solution, resulted in non-spherical clusters that had a porous and open morphology. This suggests that recrystallization and direct addition of palladium are less dominant in the case with HCl. We present two hypotheses for explaining the role of HCl in impeding the recrystallization and direct addition processes.

1. It is known that at pH < 5, $PdCl_4^{2-}$ is the dominant Pd (II) species, and the concentration of this complex ion decays sharply in the 6-10 pH range, with a parallel increase in the concentration of hydroxide-containing Pd (II) species[32]. In both solutions used for in situ electrodeposition, with pH of 2.0 for 5 mM H_2PdCl_4 and 1.6 for 5 mM H_2PdCl_4 in 0.015 M HCl, $PdCl_4^{2-}$ is the dominant species. The dissociation of $PdCl_4^{2-}$ results in the generation of adsorbed $PdCl_2$ species, which favours chloride ion adsorption at the electrode[33]. The adsorption of chloride is enhanced in the solution with HCl with increased chloride ions. We expect this to result in the retardation of direct palladium addition in the presence of HCl. The inhibiting role of HCl is also evident when we compare the integrated charge calculated in solutions with and without HCl (Supplementary Figure S7). The solution without HCl consistently resulted in a larger amount of integrated charge indicating an overall increased disposition rate compared to the case with HCl.

2. We performed electrodeposition at a potential (-200 mV versus Ag/AgCl) close to the hydrogen adsorption/absorption potential (supplementary Figure S1). In this potential range, there is competition between the adsorption and absorption of hydrogen species and the direct attachment of palladium atoms[60]. We expect this competition to be enhanced in the electrolyte with a lower pH, and to decrease the direct addition of palladium atoms in the HCl-containing solution.

The first hypothesis was further validated by replacing HCl with KCl and keeping all other conditions the same (Supplementary Figure S8). The non-spherical morphology was seen in the clusters deposited using both chloride-containing electrolytes, confirming that chloride ions are important for creating non-spherical clusters with a porous and open morphology. Comparing the chronomaperomagrams obtained in solutions with HCl and KCl indicates that HCl yields a lower

deposition rate compared to KCl. This indicates that our second hypothesis, competition between hydrogen adsorption/absorption with palladium attachment, also plays a role in tuning the reaction kinetics and potentially the nanocluster morphology.

Conclusions

We studied the role of HCl in the structural evolution of palladium electrodeposits using liquid cell TEM and *post situ* SEM analyses. We found that aggregative electrochemical growth, based on self-limiting growth, surface diffusion, and recrystallization, explained the current time transients and the electron microscopy images obtained here. The addition of HCl in the electrodeposition bath transformed the morphology of palladium electrodeposits from non-porous and closed clusters with a circular projection to porous and open clusters with a non-spherical morphology. It is evident that HCl hinders the recrystallization of aggregated nanoclusters. We hypothesize this to be related to the adsorption of chloride ions and/or the competition between palladium adatom addition and hydrogen adsorption in the presence of HCl. Combining *in situ* and the *post situ* analyses provides valuable insight into the complex phenomena that occur during electrodeposition.

Experimental

Reagents

All chemicals were obtained in the highest available purity and used without further purification. Palladium (II) chloride powder (≥99.9%) and hydrochloric acid (ACS reagent, 37%) were purchased from Sigma-Aldrich, Saint Louis, MO, USA. H_2PdCl_4 solutions were created by dissolving the palladium (II) chloride powder in HCl, and diluting the mixture in water followed by four hours of sonication. Electrolyte solutions were bubbled using nitrogen gas for 20 minutes to remove dissolved oxygen before *in situ* electrodeposition.

In situ liquid electrochemical TEM (LEC-TEM) system

The *in situ* liquid electrochemical TEM system (Poseidon 500, Protochips Inc., Raleigh, NC, USA) used in this study was composed of a liquid cell at the tip of a TEM holder. The TEM holder included electrical and fluidic circuitry for interfacing the liquid cell with a potentiostat (Gamry Reference 600, Gamry Instruments Inc., Warminster, PA, USA) for electrochemical control and a syringe pump (Harvard 11 Elite standard infuse only syringe pump, Harvard Apparatus Inc., Holliston, MA, USA) for fluidic control. Two microfabricated chips with 50 nm silicon nitride membranes were sealed inside the liquid cell and in situ imaging was performed with electrons passing through the overlapped membranes. The commercially-available bottom chip (ECT24-CO, Protochips Inc., Raleigh, NC, USA) was used as a miniaturized electrochemical cell with carbon working electrode, Pt reference electrode, and Pt counter electrode and had 500 nm spacers. The top chip only contained SiN windows (EPB-52DF, Protochips Inc., Raleigh, NC, USA) with 150 nm spacers.

In situ electron microscopy and electrodeposition

In situ chronoamperometry was performed in 5 mM H_2PdCl_4 with 0.015 M HCl and without HCl with solution flow rate of 5 μL/min. The current transients were obtained using the Gamry potentiostat. Real-time imaging was performed using a JEOL 2010F TEM operated at 200 kV. Bright-field scanning transmission electron microscope (BF-STEM) mode was performed under a beam dose of 21 electrons/frame. nm^2. In situ images were acquired using a DigiScan II (Gatan, model 788) unit with a BF detector with time resolution of 0.555 s/frame. The *in situ* process was recorded as a video and *in situ* images were extracted from the videos. The experiments were performed using a flow rate of 5 μL/min. Assuming a constant cross sectional area for the fluid

having a width of 600 μm and a minimum thickness of 0.5 μm (imposed by the spacer dimension), we estimate the upper bound for the linear flow velocity to be 278 mm/s.

Simulation and particle analysis

Simulation of electric field distribution was conducted using COMSOL Multiphysics 4.3b (COMSOL Inc., Stockholm, Sweden) by applying Tertiary Current Distribution module, which considers mass transport through diffusion and migration through Nernst-Plank equation. Measurement of the diameter and size distribution of palladium particles was performed using ImageJ.

***Post situ* analysis**

The *post situ* characterization of the structures grown on the carbon microelectrode was performed using the JEOL 7000 field emission SEM. The chips with the electrodeposited material were rinsed in DI water and air dried prior to analysis.

Supporting Information

- Figure S1 shows the *in situ* cyclic voltammogram of carbon electrode in solutions with and without HCl.
- Figure S2 shows simulation of the electric field distribution around the carbon working electrode used in liquid cell TEM experiments.
- Figure S3 shows the *in situ* chronoamperogram with electron beam on and off.
- Figure S4 shows the *in situ* chronoamperogram with the solution under static and flow conditions.
- Figure S5 shows the in *situ* chronoamperogram and *post* situ SEM images acquired in 5 mM H_2PdCl_4 solutions with 0.015 M HCl versus 0.5 M KCl.
- Figure S6 shows the size distribution of deposited palladium particles on carbon electrode used in liquid cell transmission electron microscopy in solutions with and without HCl.
- Figure S7 shows the integrated charge obtained from *in situ* chronoamperograms in 5 mM H_2PdCl_4 with and without HCl.
- Figure S8 shows the in *situ* chronomaperogram, in *situ* TEM images and post *situ* SEM images acquired in 5 mM H_2PdCl_4 solutions with 0.015 M HCl versus 0.015 M KCl.
- Supplementary Video 1 shows *in situ* electrodeposition in a solution of 5 mM H_2PdCl_4.
- Supplementary Video 2 shows *in situ* electrodeposition in a solution of 5 mM H_2PdCl_4 with 0.015 M HCl.

Acknowledgement

We acknowledge financial support from Natural Sciences and Engineering Research Council (NSERC). L.S. is the Canada Research Chair in Miniaturized Biomedical Devices, and G.A.B. is the Canada Research Chair in Microscopy of Nanoscale Materials. Both Chairs are supported by the Canada Research Chairs Program. The microscopy work was carried out at the Canadian Centre for Electron Microscopy, a facility supported by the Canada Foundation for Innovation under the Major Science Initiative program, NSERC and McMaster University.

We also acknowledge Glynis de Silveira, Andreas Korinek, and Andy Duft for assistance with experimental establishment and discussions on image analysis.

References

(1) Zhu, G.-Z.; Prabhudev, S.; Yang, J.; Gabardo, C. M.; Botton, G. a.; Soleymani, L. In Situ Liquid Cell TEM Study of Morphological Evolution and Degradation of Pt–Fe Nanocatalysts During Potential Cycling. *J. Phys. Chem. C* **2014**, *118*, 22111–22119.

(2) Gabardo, C. M.; Yang, J.; Smith, N. J.; Adams-McGavin, R. C.; Soleymani, L. Programmable Wrinkling of Self-Assembled Nanoparticle Films on Shape Memory Polymers. *ACS Nano* **2016**, *10*, 8829–8836.

(3) Soleymani, L.; Fang, Z.; Sargent, E. H.; Kelley, S. O. Programming the Detection Limits of Biosensors through Controlled Nanostructuring. *Nat. Nanotechnol.* **2009**, *4*, 844–848.

(4) Hu, Y.; Jin, J.; Wu, P.; Zhang, H.; Cai, C. Graphene-Gold Nanostructure Composites Fabricated by Electrodeposition and Their Electrocatalytic Activity toward the Oxygen Reduction and Glucose Oxidation. *Electrochim. Acta* **2010**, *56*, 491–500.

(5) Soleymani, L.; Fang, Z.; Kelley, S. O.; Sargent, E. H. Integrated Nanostructures for Direct Detection of DNA at Attomolar Concentrations. *Appl. Phys. Lett.* **2009**, *95*, 143701.

(6) González, A. L.; Noguez, C.; Barnard, A. S. Map of the Structural and Optical Properties of Gold Nanoparticles at Thermal Equilibrium. *J. Phys. Chem. C* **2012**, *116*, 14170–14175.

(7) Tian, Y.; Liu, H.; Zhao, G.; Tatsuma, T. Shape-Controlled Electrodeposition of Gold Nanostructures. *J. Phys. Chem. B* **2006**, *110*, 23478–23481.

(8) Pavlovski, J.; Myrskog, S.; Dufour, P.; Gabardo, C. M.; Soleymani, L. Fabrication of Hemispherical and Gradient-Index ZnO Nanostructures and Their Integration into Microsystems. *J. Electrochem. Soc.* **2015**, *162*, D503–D508.

(9) Gabardo, C. M.; Adams-McGavin, R. C.; Fung, B. C.; Mahoney, E. J.; Fang, Q.; Soleymani, L. Rapid Prototyping of All-Solution-Processed Multi-Lengthscale Electrodes Using Polymer-Induced Thin Film Wrinkling. *Sci. Rep.* **2017**, *7*, 42543.

(10) Jiang, Y.; Wang, Z.; Yu, X.; Shi, F.; Xu, H.; Zhang, X.; Smet, M.; Dehaen, W. Self-Assembled Monolayers of Dendron Thiols for Electrodeposition of Gold Nanostructures: Toward Fabrication of Superhydrophobic/Superhydrophilic Surfaces and PH-Responsive Surfaces. *Langmuir* **2005**, *21*, 1986–1990.

(11) Wiley, B.; Sun, Y. G.; Xia, Y. N. Synthesis of Silver Wanostructures with Controlled Shapes and Properties. *Acc. Chem. Res.* **2007**, *40*, 1067–1076.

(12) Martín-González, M.; Snyder, G. J.; Prieto, A. L.; Gronsky, R.; Sands, T.; Stacy, A. M. Direct Electrodeposition of Highly Dense 50 Nm Bi2Te 3-YSey Nanowire Arrays. *Nano Lett.* **2003**, *3*, 973–977.

(13) Chen, L.; Tang, Y.; Wang, K.; Liu, C.; Luo, S. Direct Electrodeposition of Reduced Graphene Oxide on Glassy Carbon Electrode and Its Electrochemical Application. *Electrochem. commun.* **2011**, *13*, 133–137.

(14) Zhu, C.; Meng, G.; Huang, Q.; Zhang, Z.; Xu, Q.; Liu, G.; Huang, Z.; Chu, Z. Ag Nanosheet-Assembled Micro-Hemispheres as Effective SERS Substrates. *Chem. Commun.* **2011**, *47*, 2709–

2711.

(15) Lin, T.-H.; Lin, C.-W.; Liu, H.-H.; Sheu, J.-T.; Hung, W.-H. Potential-Controlled Electrodeposition of Gold Dendrites in the Presence of Cysteine. *Chem. Commun.* **2011**, *47*, 2044-2046.

(16) Gabardo, C. M.; Zhu, Y.; Soleymani, L.; Moran-Mirabal, J. M. Bench-Top Fabrication of Hierarchically Structured High-Surface-Area Electrodes. *Adv. Funct. Mater.* **2013**, *23*, 3030–3039.

(17) Matsushita, M.; Sano, M.; Hayakawa, Y.; Honjo, H.; Sawada, Y. Fractal Structures of Zinc Metal Leaves Grown by Electrodeposition. *Phys. Rev. Lett.* **1984**, *53*, 286–289.

(18) Yang, Y.; Cheng, Y. F. Fabrication of Ni-Co-SiC Composite Coatings by Pulse Electrodeposition - Effects of Duty Cycle and Pulse Frequency. *Surf. Coatings Technol.* **2013**, *216*, 282–288.

(19) Nikolić, N. D.; Popov, K. I.; Pavlović, L. J.; Pavlović, M. G. The Effect of Hydrogen Codeposition on the Morphology of Copper Electrodeposits. I. the Concept of Effective Overpotential. *J. Electroanal. Chem.* **2006**, *588*, 88–98.

(20) Turner, A. P. F. Biosensors: Sense and Sensibility. *Chem. Soc. Rev.* **2013**, *42*, 3184–3196.

(21) Evans, B. R.; O'Neill, H. M.; Malyvanh, V. P.; Lee, I.; Woodward, J. Palladium-Bacterial Cellulose Membranes for Fuel Cells. *Biosens. Bioelectron.* **2003**, *18*, 917–923.

(22) Antolini, E. Palladium in Fuel Cell Catalysis. *Energy Environ. Sci.* **2009**, *2*, 915-931.

(23) Krishna Kumar, M.; Ramaprabhu, S. Palladium Dispersed Multiwalled Carbon Nanotube Based Hydrogen Sensor for Fuel Cell Applications. *Int. J. Hydrogen Energy* **2007**, *32*, 2518–2526.

(24) Hsu, H.-H.; Selvaganapathy, P. R.; Soleymani, L. Bottom-Up Top-Down Fabrication of Structurally and Functionally Tunable Hierarchical Palladium Materials. *J. Electrochem. Soc.* **2014**, *161*, D3078–D3086.

(25) Lu, G.; Zangari, G. Electrodeposition of Platinum on Highly Oriented Pyrolytic Graphite. Part I: Electrochemical Characterization. *J. Phys. Chem. B* **2005**, *109*, 7998–8007.

(26) Yanson, Y. I.; Rost, M. J. Structural Accelerating Effect of Chloride on Copper Electrodeposition.

Angew. Chemie - Int. Ed. **2013**, *52*, 2454–2458.

(27) Shao, W.; Pattanaik, G.; Zangari, G. Influence of Chloride Anions on the Mechanism of Copper Electrodeposition from Acidic Sulfate Electrolytes. *J. Electrochem. Soc.* **2007**, *154*, D201.

(28) Xu, L.; Guo, Y.; Liao, Q.; Zhang, J.; Xu, D. Morphological Control of ZnO Nanostructures by Electrodeposition. *J. Phys. Chem. B* **2005**, *109*, 13519–13522.

(29) Tsuru, Y.; Nomura, M.; Foulkes, F. R. Effects of Chloride, Bromide and Iodide Ions on Internal Stress in Films Deposited during High Speed Nickel Electroplating from a Nickel Sulfamate Bath. *J. Appl. Electrochem.* **2000**, *30*, 231–238.

(30) Arvia, A. J.; Canullo, J. C.; Custidiano, E.; Perdriel, C. L.; Triaca, W. E.; Investigaciones, D. Review Article of Metal Electrodes * Faceting. **1986**.

(31) Gimeno, Y.; Hernández Creus, A.; Carro, P.; González, S.; Salvarezza, R. C.; Arvia, A. J. Electrochemical Formation of Palladium Islands on HOPG: Kinetics, Morphology, and Growth Mechanisms. *J. Phys. Chem. B* **2002**, *106*, 4232–4244.

(32) Wojnicki, M.; Pacławski, K.; Rudnik, E.; Fitzner, K. Kinetics of Palladium(II) Chloride Complex Reduction in Aqueous Solutions Using Dimethylamineborane. *Hydrometallurgy* **2011**, *110*, 56–61.

(33) Gimeno, Y.; Hernández Creus, A.; Carro, P.; González, S.; Salvarezza, R. C.; Arvia, A. J. Electrochemical Formation of Palladium Islands on HOPG: Kinetics, Morphology, and Growth Mechanisms. *J. Phys. Chem. B* **2002**, *106*, 4232–4244.

(34) Schneider, N. M.; Hun Park, J.; Grogan, J. M.; Kodambaka, S.; Steingart, D. a.; Ross, F. M.; Bau, H. H. Visualization of Active and Passive Control of Morphology during Electrodeposition. *Microsc. Microanal.* **2014**, *20*, 1530–1531.

(35) Den Heijer, M.; Shao, I.; Radisic, A.; Reuter, M. C.; Ross, F. M. Patterned Electrochemical Deposition of Copper Using an Electron Beam. *APL Mater.* **2014**, *2*.

(36) Radisic, A.; Vereecken, P. M.; Hannon, J. B.; Searson, P. C.; Ross, F. M. Quantifying

Electrochemical Nucleation and Growth of Nanoscale Clusters Using Real-Time Kinetic Data. *Nano Lett.* **2006**, *6*, 238–242.

(37) Radisic, A.; Vereecken, P. M.; Searson, P. C.; Ross, F. M. The Morphology and Nucleation Kinetics of Copper Islands during Electrodeposition. *Surf. Sci.* **2006**, *600*, 1817–1826.

(38) Radisic, A.; Ross, F. M.; Searson, P. C. In Situ Study of the Growth Kinetics of Individual Island Electrodeposition of Copper. *J. Phys. Chem. B* **2006**, *110*, 7862–7868.

(39) Yang, J.; Andrei, C. M.; Botton, G. A.; Soleymani, L. In Liquid Observation and Quantification of Nucleation and Growth of Gold Nanostructures Using in Situ Transmission Electron Microscopy. *J. Phys. Chem. C* **2017**, *121*, 7435–7441.

(40) Egawa, M.; Ishida, T.; Jalabert, L.; Fujita, H. In-Situ Realtime Monitoring of Nanoscale Gold Electroplating Using Micro-Electro- Mechanical Systems Liquid Cell Operating in Transmission Electron Microscopy In-Situ Realtime Monitoring of Nanoscale Gold Electroplating Using Micro-Electro-Mechanical Syst. *Appl. Phys. Lett.* **2016**, *108*.

(41) Yang, J.; Andrei, C. M.; Botton, G. A.; Soleymani, L. In Liquid Observation and Quantification of Nucleation and Growth of Gold Nanostructures Using in Situ Transmission Electron Microscopy. *J. Phys. Chem. C* **2017**, *121*, 7435–7441.

(42) White, E. R.; Singer, S. B.; Augustyn, V.; Hubbard, W. A.; Mecklenburg, M.; Dunn, B.; Regan, B. C. In Situ Transmission Electron Microscopy of Lead Dendrites and Lead Ions in Aqueous Solution. *ACS Nano* **2012**, *6*, 6308–6317.

(43) Scharifker, B.; Hills, G. Theoretical and Experimental Studies of Multiple Nucleation. *Electrochim. Acta* **1983**, *28*, 879–889.

(44) Schneider, N. M.; Park, J. H.; Grogan, J. M.; Steingart, D. A.; Bau, H. H.; Ross, F. M. Nanoscale Evolution of Interface Morphology during Electrodeposition. *Nat. Commun.* **2017**, *8*, 1–10.

(45) Hussein, H. E. M.; Maurer, R. J.; Amari, H.; Peters, J. J. P.; Meng, L.; Beanland, R.; Newton, M. E.;

Macpherson, J. V. Tracking Metal Electrodeposition Dynamics from Nucleation and Growth of a Single Atom to a Crystalline Nanoparticle. *ACS Nano* **2018**, *12*, 7388–7396.

(46) Ustarroz, J.; Hammons, J. A.; Altantzis, T.; Hubin, A.; Bals, S.; Terryn, H. A Generalized Electrochemical Aggregative Growth Mechanism. *J. Am. Chem. Soc.* **2013**, *135*, 11550–11561.

(47) Ustarroz, J.; Ke, X.; Hubin, A.; Bals, S.; Terryn, H. New Insights into the Early Stages of Nanoparticle Electrodeposition. *J. Phys. Chem. C* **2012**, *116*, 2322–2329.

(48) Kim, Y. R.; Lai, S. C. S.; McKelvey, K.; Zhang, G.; Perry, D.; Miller, T. S.; Unwin, P. R. Nucleation and Aggregative Growth of Palladium Nanoparticles on Carbon Electrodes: Experiment and Kinetic Model. *J. Phys. Chem. C* **2015**, *119*, 17389–17397.

(49) Mamme, M. H.; Köhn, C.; Deconinck, J.; Ustarroz, J. Numerical Insights into the Early Stages of Nanoscale Electrodeposition: Nanocluster Surface Diffusion and Aggregative Growth. *Nanoscale* **2018**, *10*, 7194–7209.

(50) Guo, L.; Searson, P. C. On the Influence of the Nucleation Overpotential on Island Growth in Electrodeposition. *Electrochim. Acta* **2010**, *55*, 4086–4091.

(51) Ahmad, N.; Le Bouar, Y.; Ricolleau, C.; Alloyeau, D. Growth of Dendritic Nanostructures by Liquid-Cell Transmission Electron Microscopy: A Reflection of the Electron-Irradiation History. *Adv. Struct. Chem. Imaging* **2017**, *2*, 9.

(52) Schneider, N. M.; Norton, M. M.; Mendel, B. J.; Grogan, J. M.; Ross, F. M.; Bau, H. H. Electron-Water Interactions and Implications for Liquid Cell Electron Microscopy. *J. Phys. Chem. C* **2014**, *118*, 22373–22382.

(53) Mehdi, B. L.; Qian, J.; Nasybulin, E.; Park, C.; Welch, D. A.; Faller, R.; Mehta, H.; Henderson, W. A.; Xu, W.; Wang, C. M.; *et al.* Observation and Quantification of Nanoscale Processes in Lithium Batteries by Operando Electrochemical (S)TEM. *Nano Lett.* **2015**, *15*, 2168–2173.

(54) Mehdi, B. L.; Stevens, A.; Qian, J.; Park, C.; Xu, W.; Henderson, W. A.; Zhang, J. G.; Mueller, K. T.;

Browning, N. D. The Impact of Li Grain Size on Coulombic Efficiency in Li Batteries. *Sci. Rep.* **2016**, *6*, 1–8.

(55) Woehl, T. J.; Jungjohann, K. L.; Evans, J. E.; Arslan, I.; Ristenpart, W. D.; Browning, N. D. Experimental Procedures to Mitigate Electron Beam Induced Artifacts during in Situ Fluid Imaging of Nanomaterials. *Ultramicroscopy* **2013**, *127*, 53–63.

(56) Khan, H. M.; Waltz, W. L.; Woods, R. J. A PULSE RADIOLYSIS STUDY OF TETRAAMMINEPLATINUM (II) COMPLEX ION IN AQUEOUS CHLORIDE MEDIA. **1986**, *27*, 41–45.

(57) Bard, A. J.; Faulkner, L. R. *Electrochemical Methods: Fundamentals and Applications*; 2nd ed.; John Wiley & Son, Inc.: New York, 2001.

(58) Gunawardena, G.; Hills, G.; Montenegro, I. Electrochemical Nucleation. Part IV. Electrodeposition of Copper onto Vitreous Carbon. *J. Electroanal. Chem.* **1985**, *184*, 357–369.

(59) Redmond, P. L.; Hallock, A. J.; Brus, L. E. Electrochemical Ostwald Ripening of Colloidal Ag Particles on Conductive Substrates. *Nano Lett.* **2005**, *5*, 131–135.

(60) Jerkiewicz, G. Hydrogen Sorption at/in Electrodes. *Prog. Surf. Sci.* **1998**, *57*, 137–186.

TOC graphic

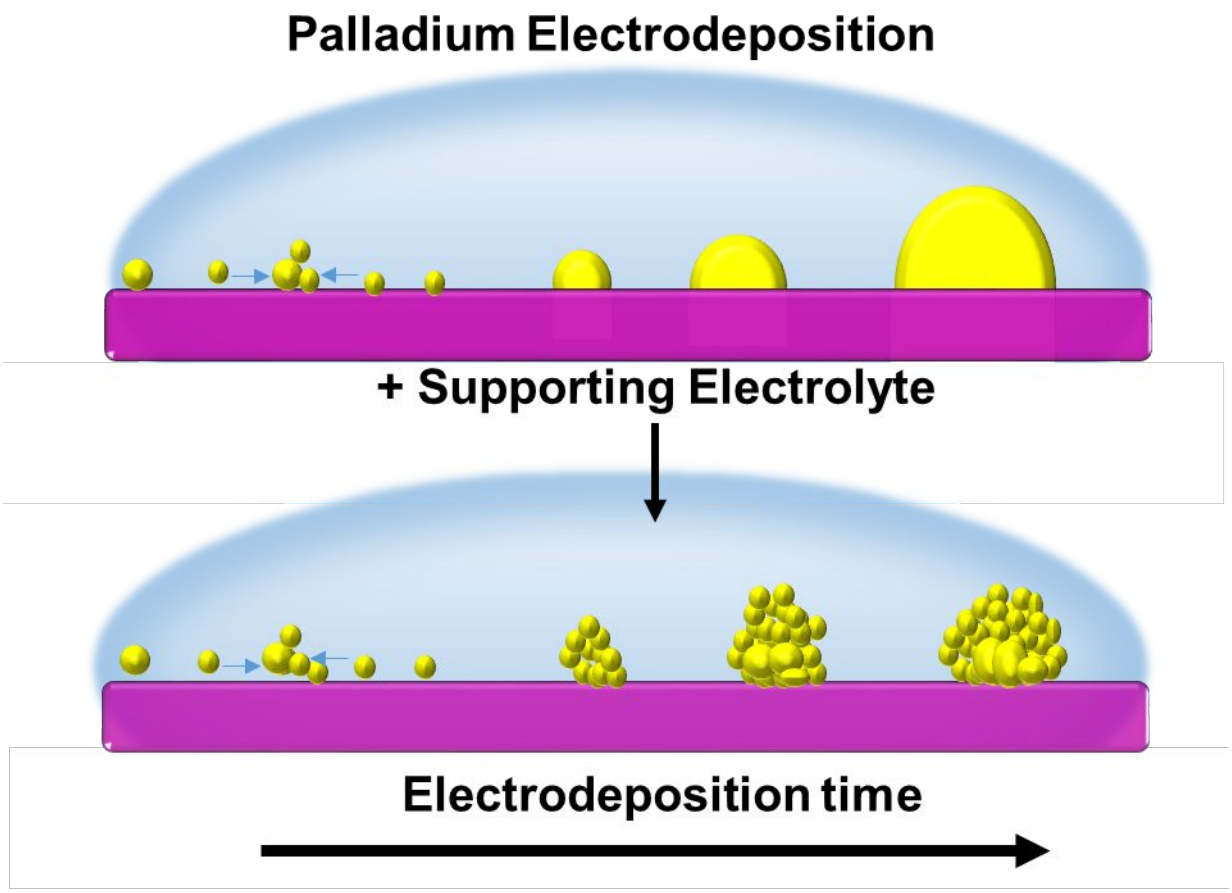
Palladium Electrodeposition
+ Supporting Electrolyte
Electrodeposition time